

Multiorgan Crystal Deposition of an Amphoteric Drug in Rats Due to Lysosomal Accumulation and Conversion to a Poorly Soluble Hydrochloride Salt

Barbara Lenz,^{*,1} Andreas Brink,^{*} Michael J. Mihatsch,[†] Bernd Altmann,^{*} Urs Niederhauser,^{*} Bernd Steinhuber,^{*} Nicole Wyttenbach,^{*} and Holger Fischer^{*}

^{*}Roche Pharma Research and Early Development, Pharmaceutical Sciences, Roche Innovation Center Basel, F. Hoffmann-La Roche Ltd, 4070 Basel, Switzerland; and [†]Pathology, Institute of Medical Genetics and Pathology, University Hospital of Basel, University of Basel, 4031 Basel, Switzerland

¹To whom correspondence should be addressed at Roche Pharma Research and Early Development, Pharmaceutical Sciences, Roche Innovation Center Basel, F. Hoffmann-La Roche Ltd, Grenzacherstrasse 124, 4070 Basel, Switzerland. E-mail: barbara.lenz@roche.com.

ABSTRACT

Poor solubility of drug candidates mainly affects bioavailability, but poor solubility of drugs and metabolites can also lead to precipitation within tissues, particularly when high doses are tested. RO0728617 is an amphoteric compound bearing basic and acidic moieties that has previously demonstrated good solubility at physiological pH but underwent widespread crystal deposition in multiple tissues in rat toxicity studies. The aim of our investigation was to better characterize these findings and their underlying mechanism(s), and to identify possible screening methods in the drug development process. Main microscopic features observed in rat RO0728617 toxicity studies were extensive infiltrates of crystal-containing macrophages in multiple organs. Matrix-assisted laser desorption/ionization Fourier transform ion cyclotron resonance mass spectrometry revealed that these crystals contained the orally administered parent compound, and locality was confirmed to be intracytoplasmic and partly intralysosomal by electron microscopic examination. Crystal formation was explained by lysosomal accumulation of the compound followed by precipitation of the hydrochloride salt under physiological conditions in the lysosomes, which have a lower pH and higher chloride concentration in comparison to the cytosol. This study demonstrates that risk of drug precipitation can be assessed by comparing the estimated lysosomal drug concentration at a given dose with the solubility of the compound at lysosomal conditions.

Key words: crystal deposition; drug precipitation; macrophages; organ toxicity; lysosomal accumulation.

Poor aqueous solubility of drug candidates is one of the major challenges in drug discovery and development (Boyd *et al.*, 2019). In the case of orally administered drugs, poor solubility of drugs and metabolites predominantly affects bioavailability, but can also lead to toxicity due to precipitation within tissues. This is particularly seen in preclinical toxicity studies where drug candidates are tested at high doses. The kidney is

especially susceptible to drug precipitation due to its filtration function (Nasr *et al.*, 2014). However, precipitates have also been described in many other tissues (Aziz and Helms 2009; Baik and Rosania 2012; Yuste *et al.*, 2017), including the eye (Nadim *et al.*, 2001). The solubility/dissolution of an organic compound depends on its physicochemical properties, which are mainly determined by inter-molecular interactions (Van der Waal

© The Author(s) 2021. Published by Oxford University Press on behalf of the Society of Toxicology.

This is an Open Access article distributed under the terms of the Creative Commons Attribution-NonCommercial-NoDerivs licence (<http://creativecommons.org/licenses/by-nc-nd/4.0/>), which permits non-commercial reproduction and distribution of the work, in any medium, provided the original work is not altered or transformed in any way, and that the work is properly cited. For commercial re-use, please contact journals.permissions@oup.com

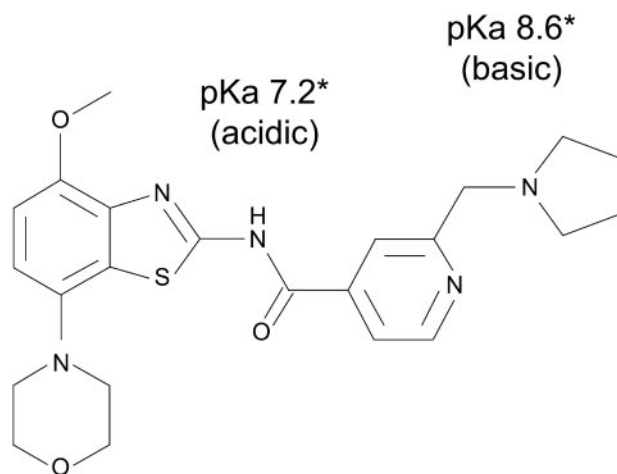


Figure 1. Chemical structure of RO0728617; an amphoteric compound. The acid dissociation constants (pKa) are given for the basic and acidic moieties. The molecular weight of RO0728617 is 453.6 g/mol, the melting point is 217°C and the LogD (pH7.4) is 1.5, as measured by the Carrier-Mediated Distribution System (Wagner et al., 2015). *Measured by photometric titration.

interactions, hydrogen bonding, etc.) of the solid form and interactions of the molecule with the surrounding solvent. It is well established that molecules in different solid forms (eg, crystalline, amorphous, salts, cocrystals, etc.) may have dissolution rates that differ by orders of magnitude. Likewise, small changes in experimental conditions can lead to significant changes in compound dissolution, such as changes in temperature, ionic strength, pH (in the case of charged compounds), buffer composition, or the presence of organic solvents (Nie et al., 2017). Similar effects exist in the opposite scenario if an organic molecule is completely dissolved; slightly altered conditions can lead to spontaneous precipitation of a compound from an initially clear solution (Brouwers et al., 2009).

It has been suggested that certain crystalline deposit-inducing compounds, such as tamoxifen or clofazimine, accumulate intracellularly, most likely within lysosomes (Keswani et al., 2015; Lüllmann and Lüllmann-Rauch, 1981). Sequestering of weakly basic drugs in acidic organelles, organelles like lysosomes (also known as lysosomal trapping), is a well-known phenomenon (Logan et al., 2012). At the low pH experienced within the lysosomes these drugs can be ionized, reducing their capacity to diffuse back into the cytosol and resulting in lysosomal accumulation. Lysosomal trapping and accumulation usually occurs with cationic amphiphilic drugs (CADs), leading to phospholipidosis; an excessive accumulation of phospholipids and drugs within lysosomes (Chatman et al., 2009).

Here, we report toxicity findings in rats seen after treatment with RO0728617; an amphoteric adenosine A2a receptor antagonist bearing basic (pKa 8.6) and weakly acidic (pKa 7.2) moieties (Figure 1), which was in preclinical development for treatment of psychiatric disorders at F. Hoffmann-La Roche. The compound was predicted to be negative for phospholipidosis *in silico* but demonstrated a weak signal for phospholipidosis *in vitro* (Fischer et al., 2012). RO0728617 also showed good solubility at physiological pH. Since widespread crystal deposition in multiple tissues was observed in rat toxicity studies, further investigations were initiated to better characterize these findings and their underlying mechanism(s), and to improve compound optimization procedures in drug discovery and early development.

MATERIALS AND METHODS

Animal studies. A 2-week oral dose range-finding study and a 4-week oral good laboratory practice (GLP) toxicity study were performed in male and female Wistar rats (CrI : [WI]BR strain or CrI: WI[Glx/BRL/Han] bred using the Charles River International Genetic Standard system, supplied at approximately 7–8 weeks of age by Charles River UK Limited, England, or Charles River Laboratories, France). To better understand the mechanism(s) of toxicity observed in the 2 toxicity studies and in parallel to validate new ophthalmologic examination and application techniques (Soukup et al., 2020), a mechanistic study consisting of 2 parts (2–4 or 8 weeks) was performed in Wistar and Brown-Norway rats obtained from Charles River Laboratories, Germany (CrI: WI[Han], CrI: BN) at the age of 8 weeks. In this mechanistic study, only male rats were included as no difference between sexes was observed in the dose range-finding and GLP toxicity studies. Rats were acclimatized for 7–14 days prior to treatment and were housed in groups of 2–4 animals (of the same sex) in stainless steel mesh cages or macrolon boxes, according to dosing group. Rats were kept on a standard 12-h light/dark cycle with pelleted food and filtered tap water supplied *ad libitum*.

Studies were performed in laboratories approved by the Association for the Assessment and Accreditation of Laboratory Animal Care, the Swiss Federal Act on Animal Protection (Swiss APA 1978), the French minister of agriculture for the use of animals for scientific purposes, and the authority of licenses granted by the U.K. Home Office. Studies were performed in accordance with Swiss Animal Protection law, the European Council Directive (86/609/EEC) of November 24, 1986 on the approximation of laws, regulations and administrative provisions of the Member States relating to the protection of animals used for experimental and other scientific purposes (JOCE, L 358, December 18, 1986), and the UK Animals (Scientific Procedures) Act 1986.

Study design and procedures. Study design and procedures are detailed in Table 1. In all studies, RO0728617 was administered by oral gavage as a crystalline suspension in an aqueous vehicle (pH 5.0) containing 2% (w/w) Avicel CL-611 and 0.2% (w/w) poly-sorbate 80 at 5 ml/kg. Doses were 0, 20, and 50 mg/kg/day in the 2-week dose range-finding study. As no maximum tolerated dose was achieved in this study, the high dose was increased in the 4-week oral GLP toxicity study, in which 0, 5, 15, 45, and 90 mg/kg/day were administered. The dose of 90 mg/kg/day was also applied in the mechanistic study, in which 90 mg/kg/day was administered for 2 or 4 weeks, or 90 mg/kg/day adjusted to 70 mg/kg/day between days 8 and 29 (due to suspected intolerance) and increased again to 90 mg/kg/day for 8 weeks. For the dose range-finding and 4-week GLP toxicity studies, animals were euthanized within 24 h after last dose for subsequent examination by exposure to rising concentrations of carbon dioxide followed by exsanguination upon a negative response to toe pinching. In the mechanistic study, animals were euthanized within 24 h after last dose by intraperitoneal injection of pentobarbital followed by exsanguination upon a negative response to toe pinching. Parameters evaluated were body weight, food consumption, clinical observations, toxicokinetic parameters, ophthalmology, clinical pathology, necropsy, organ weights, and histopathology (including special stains and immunohistochemistry [IHC]). Additional parameters included examination of frozen sections, electron microscopy (EM), and matrix-

Table 1. Design of Toxicity Studies Performed

Study	2-Week Oral Dose Range Finder	4-Week Oral GLP With 8-Week Recovery	Mechanistic (2, 4, and 8 Weeks)
Strain	Wistar rat	Wistar rat	Wistar rat and Brown Norway rat
Sex	Male and female	Male and female	Male
Number of animals/sex/groups	5	8/6 (recovery)	8/2 (8 weeks)
RO0728617 dose	0, 20, and 50 mg/kg/day	0, 5, 15, 45, and 90 mg/kg/day	90 or 90/70/90 mg/kg/day
Standard parameters	Body weight, food consumption, clinical observations, ophthalmology, clinical pathology, and necropsy	Body weight, food consumption, clinical observations, ophthalmology, clinical pathology, necropsy, and organ weights	Body weight, food consumption, clinical observations, ophthalmology, and necropsy
Histopathology	Standard tissue list for toxicity study	Standard tissue list for toxicity study	Eye, kidney, lungs, and stomach
IHC	n/a	CD68: Eye, parathyroid gland, pituitary gland, salivary gland, bone marrow, mesenteric lymph node, nasal cavity, and teeth PTH: parathyroid gland	CD68: Kidney (at weeks 2 and 4) Lamp2: Lungs (at week 4) and Kidney (at weeks 2 and 4)
Examination of frozen tissues	n/a	Eye and bone marrow (femur)	Eye, kidney, and stomach
EM	n/a	Eye	Eye and kidney
MALDI-FTICR MS imaging	n/a	n/a	Eye and stomach
Investigations separately reported (Lenz et al., 2018; Soukup et al., 2020)	n/a	n/a	cSLO, OCT imaging, Raman and infrared microspectroscopy (kidney), and SEM/EDX spectroscopy (kidney)

Abbreviations: cSLO, confocal scanning laser ophthalmoscope; GLP, good laboratory practice; Lamp2, lysosome-associated membrane protein 2; MALDI-FTICR MS, matrix-assisted laser desorption/ionization Fourier transform ion cyclotron resonance mass spectrometry; n/a, not applicable; OCT, optical coherence tomography; PTH, parathyroid hormone; SEM/EDX, scanning electron microscopy coupled with energy dispersive X-ray.

assisted laser desorption/ionization Fourier transform ion cyclotron resonance (MALDI-FTICR) mass spectrometry (MS) imaging.

Ophthalmology. In the 4-week GLP toxicity study, indirect ophthalmology was performed at pretesting on all animals by instilling with a mydriatic agent (tropicamide 1%) before examination of the posterior segment of the eye, with additional ophthalmology at week 4, and on all recovery animals once weekly during treatment-free periods (weeks 5–12). More detailed ocular examinations were performed in the mechanistic study, which was performed to validate new ophthalmological examination and application techniques. These results have been reported separately (Soukup et al., 2020).

Histopathological examination. In the 2-week dose range-finding and 4-week GLP toxicity studies, all major organs and tissues underwent histopathological evaluation at the end of the treatment period in animals from the control and high-dose groups. Target tissues were examined from intermediate dosing groups and recovery animals (4-week GLP toxicity study). In the mechanistic study, selected tissues were examined. All tissue samples were collected, preserved in 10% neutral formalin, Davidson's fluid (for eyes and testes) or Bouin's solution (testes; dose range-finding study) and stained with hematoxylin and eosin (H&E) with the exception of bone marrow smears, which were fixed in 100% methanol and stained with May Grünwald-Giemsa. Kidney sections were additionally stained with Periodic Acid Schiff. Additional stains on selected tissues included Trichrome (Martius Scarlett Blue), and IHC for Lamp2 for lysosomal membranes (51-2200, Zymed Laboratories), CD68 for

macrophages (T1005, BMA), and parathyroid hormone (NCL-PTH-OP4, Novocastra).

Examination of frozen tissues. Lungs, kidney, mesenteric lymph node, spleen, stomach, eye, and bone marrow samples were snap frozen in liquid nitrogen and stored at -80°C . Ten- μm thick unstained frozen sections were prepared from selected tissues with obvious crystal deposits in H&E staining by thawing on Superfrost glass slides (Thermo Scientific, Germany) and examined microscopically for crystal deposits under polarized light.

Electron microscopy. Samples of the lungs, stomach, kidneys, and eyes of selected animals were fixed in Karnovsky fixative or 3.5% glutaraldehyde, then postfixed with 1% osmium tetroxide and embedded in plastic. Electron microscopic examination was performed on selected eyes from all groups of the 4-week GLP toxicity study and selected eyes and kidneys from the mechanistic study using a JEOL JEM-1400 Flash Electron Microscope or Morgagni 268 D (FEI Company, Hillsboro, Oregon).

MALDI-FTICR MS imaging. Tissues sections that showed presence of birefringent crystal deposits at light microscopic examination were further processed by MALDI-FTICR MS imaging; tissue sections on Superfrost glass slides were scanned with an Aperio ScanScope slide scanner (ScanSope AT) and processed for MALDI-FTICR MS analysis. For coating the tissue slide with matrix, a solution of α -cyano-4-hydroxycinnamic acid at 10 mg/ml in 1:1 acetonitrile:0.1% 2,2,2-trifluoroethanoic acid in water was applied using an iMatrixSpray sprayer (Stoeckli et al., 2014). Four spraying cycles were applied at a flow rate of $5\ \mu\text{l}/\text{cm}^2$. Tissue samples were analyzed on a 7 Tesla Solarix XR FTICR MS

instrument with a MALDI source equipped with a Smartbeam-II Laser System (Bruker, Bremen, Germany). Ions were detected in positive ionization mode over a mass range of 150–3000 m/z, with a lateral resolution of 10 μm . Two hundred laser shots using sequential settings were applied per pixel at 2000 Hz, with laser power at 20%. The signal for each pixel was normalized against the root mean square of all data points. The ion image was coregistered with an optical scan generated from the tissue slide before MS imaging using an optical scanner (OpticLab H850, Plustek, Germany). All MS images were generated with Fleximaging 4.0 software (Bruker, Bremen, Germany). Compound RO0728617 was identified by matching measured m/z values with the value calculated based on its elemental formulae ($\text{C}_{23}\text{H}_{27}\text{N}_5\text{O}_3\text{S}$), within a mass window of 1 ppm.

Determination of drug solubility. The solubility of RO0728617 (free form) and of RO0728617-hydrochloride (HCl) salt was determined using a modified miniaturized *in situ* salt screening (InSiSa) method, as previously described (Tong and Whitesell, 1998). Details of this method can be found in the [Supplementary Material](#).

Estimation of concentration in lysosomes based on the total plasma concentration. Lysosomal concentration was estimated based on the pH-partition hypothesis and the free drug hypothesis, as previously described (Friden et al., 2011). The free concentration in the lysosomes was calculated by a 3-compartment model. Details of this calculation process can be found in the [Supplementary Material](#).

RESULTS

In-Life Observations

In the 2-week dose range-finding study there were no clinical signs or effects on bodyweight or food consumption in the animals after dosing with RO0728617. At 90 mg/kg/day in the 4-week GLP toxicity study and in the mechanistic study, animals were noted to have lower bodyweight gain and food consumption compared with control animals.

Ophthalmology

Multifocal spots in the fundus occasionally associated with fundus brightness were noted in animals from the 90 mg/kg/day group of the 4-week GLP toxicity study. Fundus changes were observed bilaterally in almost all cases, with a similar incidence between males and females but were generally more severe in females compared with males. The severity of this change decreased throughout the treatment-free period but was not completely reversed by the end of the 8-week recovery period. No such changes were observed with lower doses, or in control animals. Similar changes were observed in the mechanistic study (Soukup et al., 2020), where doses comparable with the high dose in the 4-week GLP toxicity study were administered.

Histopathological Examination

In the 2-week toxicity study, the only compound-related finding was a foamy or vacuolated macrophage accumulation in the lungs of animals in the 50 mg/kg/day group. Foamy/vacuolated macrophage accumulation in the lungs was also observed at 45 mg/kg/day (comparable with the high dose administered in the 2-week toxicity study) and 90 mg/kg/day of the 4-week toxicity study (Figure 2A). Lamp2 immunostaining of lungs in the mechanistic study revealed strong positive staining of

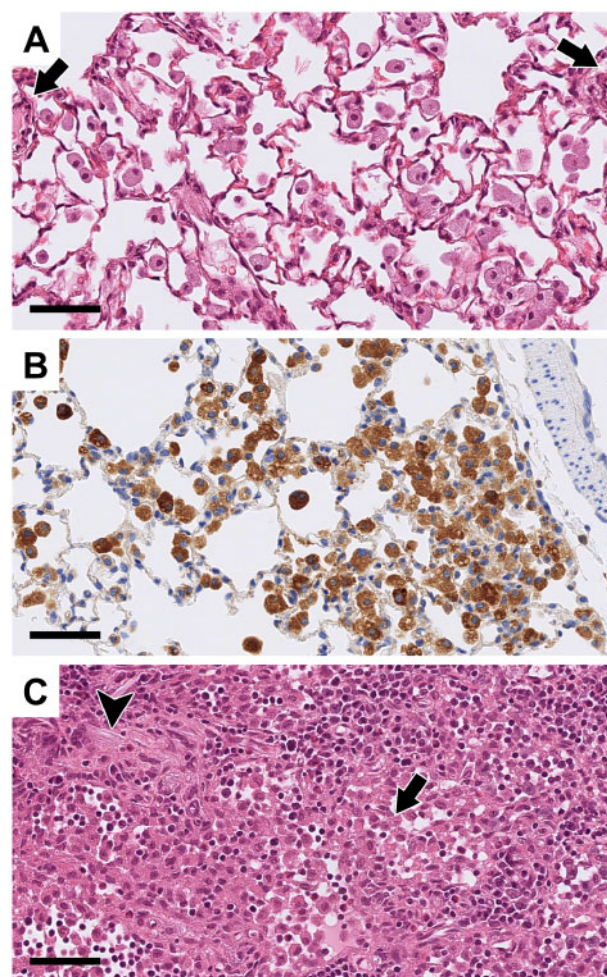


Figure 2. Histopathological examination. A, hematoxylin and eosin (H&E) stain of a lung from a female rat treated with RO0728617 at 90 mg/kg/day for 28 days showing enlarged intra-alveolar macrophages with vacuolated cytoplasm. Arrows show unchanged vessels. B, Lamp2 immunohistochemistry of a lung from a male rat treated with 90 mg/kg/day RO0728617 for 28 days in the mechanistic study, showing strong positive staining of cytoplasmic vacuoles in alveolar macrophages. Note: no sex differences were observed between (A and B). C, H&E stain of mesenteric lymph node from a female rat treated with 90 mg/kg/day for 28 days showing foamy macrophages in sinusoids (arrow), and single macrophages with intracytoplasmic crystal clefts (arrowhead). Scale bars = 50 μm .

cytoplasmic vacuoles in alveolar macrophages (Figure 2B), confirming their association with lysosomes. In addition, foamy/vacuolated macrophage accumulation within the lymph nodes (Figure 2C) and vacuolated Kupffer cells in the liver were also observed at ≥ 45 and 90 mg/kg/day, respectively, in the 4-week toxicity study. The major compound-related finding after treatment at ≥ 45 mg/kg/day for 4 weeks; however, was the presence of crystal deposits in multiple organs, particularly in the parathyroid glands, bone marrow, pulp of the teeth, lymph nodes, spleen, salivary and pituitary glands, kidneys, and eyes at the end of the treatment period. In the hematoxylin and eosin stain, areas of fibrillary structures with scattered nuclei were noted in the tissues, corresponding to macrophage infiltrates with crystal clefts in the cytoplasm (Figs. 2C–5); this was confirmed by immunostaining with anti-CD68 in the kidneys (Figs. 4D and 4E), bone marrow (Figure 3B), parathyroid glands (Figure 3D), salivary glands, nasal cavity, teeth pulp, mesenteric lymph

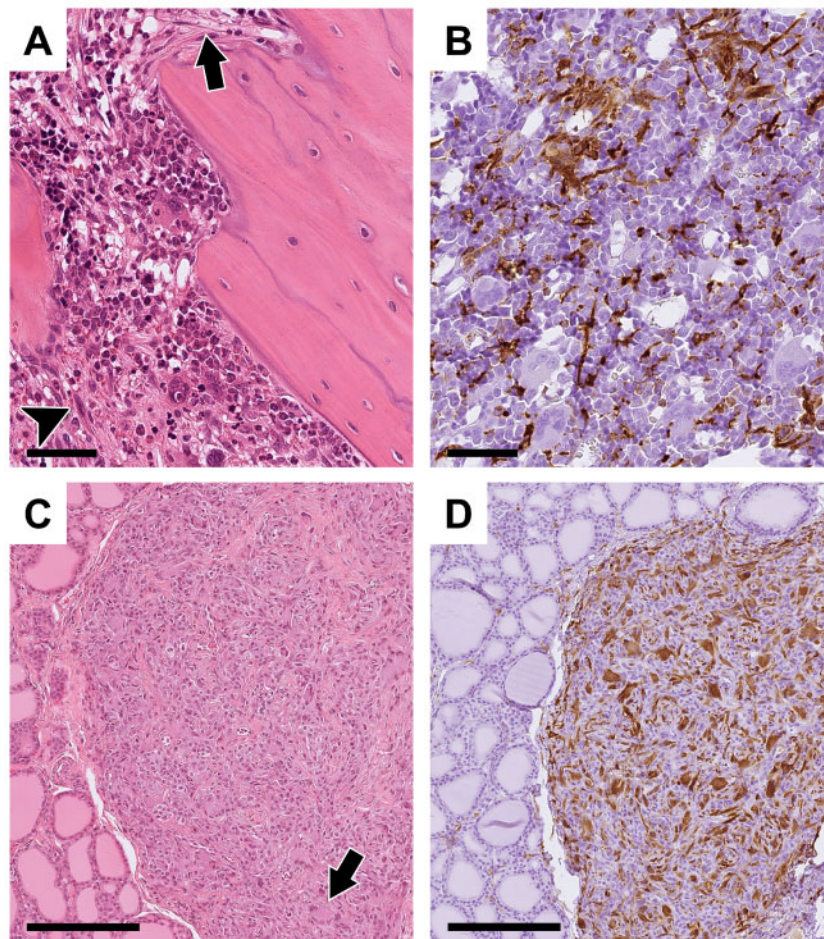


Figure 3. Macrophage infiltrates of the bone marrow and parathyroid gland. A, hematoxylin and eosin (H&E) stain of bone marrow from the tibia of a male rat treated with RO0728617 at 90 mg/kg/day for 28 days showing macrophage infiltrates (arrowhead) with crystal clefts (arrow), and immunostaining with anti-CD68 confirming presence of macrophages in the bone marrow (B). Scale bars = 50 μ m. C, H&E stain of parathyroid gland of a male rat treated with 90 mg/kg/day RO0728617 for 28 days shows normal parathyroid gland replaced by infiltrates of elongated macrophages containing crystal clefts, with occasional multinucleated cells (arrow). The surrounding thyroid gland is largely unchanged. Immunostaining with anti-CD68 confirms the presence of macrophages in the parathyroid gland (D). Scale bars = 200 μ m.

nodes, and pituitary glands of animals in the highest dose group of the 4-week toxicity study. This finding was also associated with a pale discoloration of some tissues. Macrophage infiltrates were extensive in some tissues, partially replacing bone marrow, causing loss of parathyroid gland structure, and were accompanied by inflammation of the mesenteric lymph node capsule.

Parathyroid tissue could only be confirmed to contain parathyroid cells by parathyroid hormone IHC. In the spleen, the red pulp was affected and in 1 animal, macrophage infiltrates were associated with focal necrosis. Macrophage infiltrates with crystal deposits were also seen throughout the pituitary gland. In the kidney, macrophage infiltrates with crystal deposits were mainly seen in the interstitium of the deep cortex and the outer medulla (Figs. 4A, 4D, and 4E). Tubular degeneration and regeneration with mitoses and nuclear enlargement were present in some areas of the kidneys (Figure 4B). Crystals were not found in tubules, or glomeruli (Figure 4C).

Changes observed in the eyes involved the retina (particularly the retinal pigment epithelium), the choroid and the ciliary bodies, which also revealed macrophage infiltrates and crystal deposits. In the retina, the nuclei of the pigment epithelium were abnormal in shape and/or size, often with a prominent

nucleolus. In individual rats there were granuloma formation (Figure 5A) and mitotic figures. Other changes in the retina consisted of folds, with an apparent thinning of the external photoreceptor layer and thinning of the outer nuclear cell layer (Figure 5A). Macrophage infiltrates in the retina, choroid and ciliary bodies, were confirmed by immunostaining with anti-CD68 (Figure 5B). One female rat in the 45 mg/kg/day group displayed abnormally enlarged nuclei of the pigment epithelium.

In addition to the described crystal deposits in various tissues, loss of parietal cells as well as an increased number of mucous cells, was also observed in the fundic mucosa of the glandular stomach.

Similar changes were seen in the mechanistic study. However, in this toxicity study, CD68 immunostaining of the kidney revealed macrophage infiltrates after just 2 weeks of treatment at 90 mg/kg/day. An increase in macrophage infiltration was mainly observed interstitially within the medulla. Macrophages were often rounded, and there were occasionally elongated macrophages with crystal clefts observed interstitially, and single-elongated macrophages observed intravascularly. Lamp2 IHC showed that crystal clefts were frequently surrounded by Lamp2-positive structures (Figure 4G). Lamp2 IHC of the kidneys of animals from the 2- and 4-week sacrifice

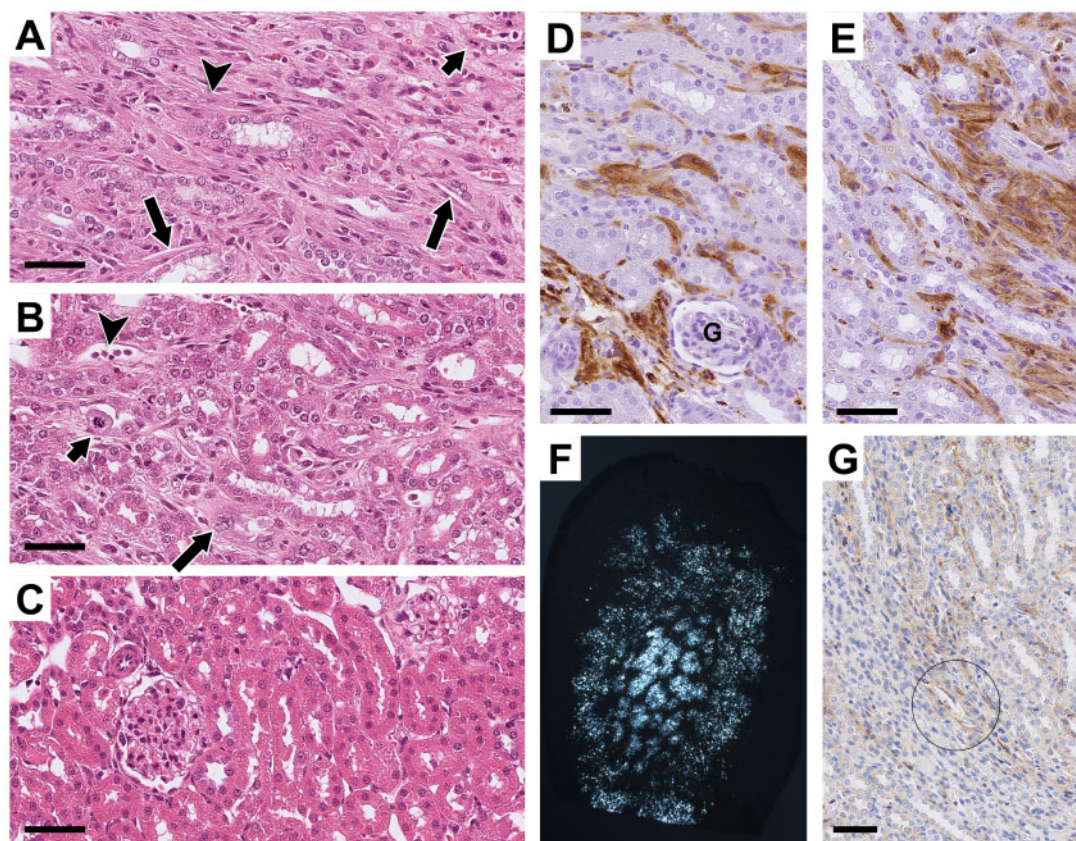


Figure 4. Histopathological examination of the kidney. In the kidney of a female rat treated with RO0728617 at 90 mg/kg/day for 28 days, hematoxylin and eosin staining shows interstitial infiltrates of elongated, spindle-shaped macrophages (arrowhead) with crystal clefts (long arrows), and tubular cells with mitotic figures (short arrow, A). B, Tubules reveal degeneration and regeneration with mitoses (short arrow) and nuclear enlargement (long arrow); (dilated peritubular capillaries with increased number of mononuclear cells [arrowhead]). C, Normal cortex with unchanged glomeruli, arteries and capillaries. In the kidney of a male rat treated with RO0728617 at 90 mg/kg/day for 28 days, immunostaining with anti-CD68 confirms the presence of macrophages, with no crystals in the glomeruli (G) or tubules (D and E). Scale bars = 50 μ m. Note: there were no sex differences between (A and E). F, In an unstained frozen section, massive crystal deposition in the renal medulla can be observed with polarized light. Note: no crystal deposits are present in the renal cortex. G, In the kidney of a male rat treated for 14 days (mechanistic study), immunostaining with anti-Lamp2 shows that crystal clefts within interstitial infiltrates are surrounded by positive membranes (encircled). Scale bar = 60 μ m.

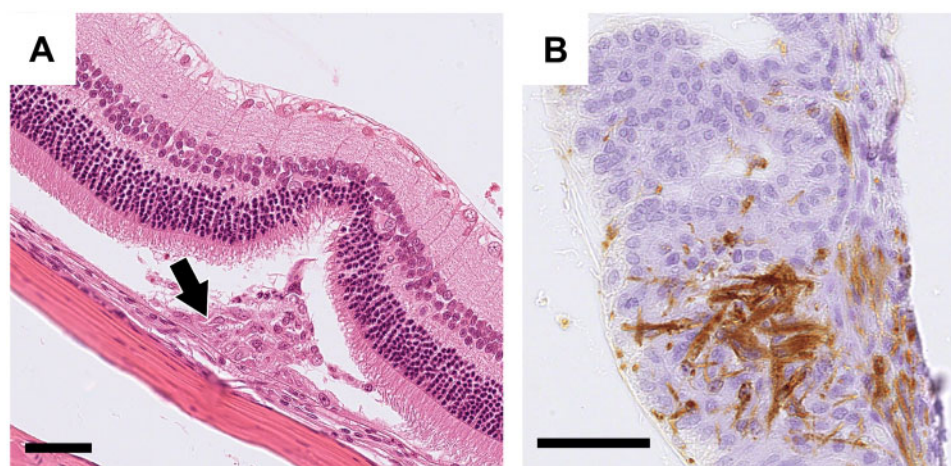


Figure 5. Histopathological examination of the eye. A, hematoxylin and eosin stain of the eye from a male rat treated with RO0728617 at 90 mg/kg/day for 28 days showing a subretinal cell cluster (likely to be macrophages) with crystal clefts (arrow) and retinal infolding. Note that adjacent tissue is unchanged. B, CD68 IHC of the eye from a female rat treated with RO0728617 at 90 mg/kg/day for 28 days showing the ciliary body with macrophage infiltrates and intracytoplasmic crystal clefts. Scale bars = 50 μ m.

did not reveal any difference in positive staining of tubular cells between control and treated rats. The microscopic findings in the mechanistic study were not strain specific; Brown-Norway

rats treated at a dose of 90 mg/kg/day for 2–4 weeks showed similar changes to Wistar rats. Microscopic images of control animals are shown in [Supplementary Figure 1](#).

Examination of Frozen Tissues

The presence of birefringent crystals of approximately 5–10 μm in length was confirmed under polarized light within the retina (pigment epithelium; Figure 6A) and the ciliary body, within the bone marrow, stomach mucosa, and kidneys (Figure 4F). In the stomach mucosa, crystals were mainly observed in the middle third of the mucosa. In the kidneys, crystals were interstitially located.

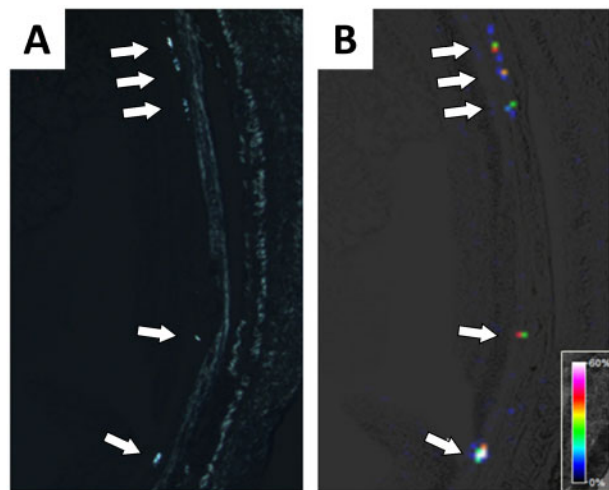


Figure 6. Molecular imaging of crystal deposits by matrix-assisted laser desorption/ionization Fourier transform ion cyclotron resonance (MALDI-FTICR) mass spectrometry (MS) in the eye of a male rat treated with RO0728617 at 90/70/90 mg/kg/day for 8 weeks. A, Polarized light microscopy image of the retina before MS image analysis visualizing crystal deposits (white arrows). B, Overlay of MALDI-FTICR MS image of the same retinal section with an optical scan to visualize spatial distribution of 454.1907 m/z, with a mass accuracy of <1 ppm, the protonated form of the parent compound orally administered to the animal.

Electron Microscopy

The presence of crystal deposits was also confirmed by EM of the eyes and kidneys. In the eye, crystal clefts were predominantly observed in the pigment epithelium of the retina; some clefts were within melanosomes and others seemed to be surrounded by membranes, suggestive of lysosomal localization (Figure 7A). The kidney revealed numerous interstitial cells with crystal clefts, often densely packed. In contrast to the eyes, membranes surrounding the crystals in the kidneys were not unequivocally found (Figure 7B). Peritubular macrophages with crystal clefts and occasional interstitial giant cells were also observed in the kidneys. Crystals were approximately 5–10 μm in length and approximately 275 nm in width; occasionally, crystals were >10 μm long. No evidence of crystals could be found in glomeruli, tubular cells nor blood vessels.

MALDI-FTICR MS Imaging

MALDI-FTICR MS imaging demonstrated that the crystals identified within rat retina were composed of the administered parent drug. In Figure 6, crystal deposits in retina are visualized by light microscopy (Figure 6A), with an additional overlay of the same region showing the respective MALDI-FTICR MS image to visualize the spatial distribution of RO0728617 (Figure 6B). The mass signal of 454.1907 m/z, with a mass accuracy of <1 ppm corresponding to the protonated form of parent drug detected by MALDI imaging, clearly demonstrates colocalization with the crystals observed by light microscopy, whereas other areas of the retina showed no presence of the parent drug. Further examination of rat kidney and stomach tissue confirmed an association of tissue regions that contained birefringent crystal deposits with the administered parent drug.

Drug Solubility

The aqueous solubility of RO0728617 (free form) was estimated to be 0.149 mg/ml at pH 7.4 and 32.2 mg/ml at pH 5.0 (Figure 8). The estimated solubility of RO0728617 at lysosomal chloride

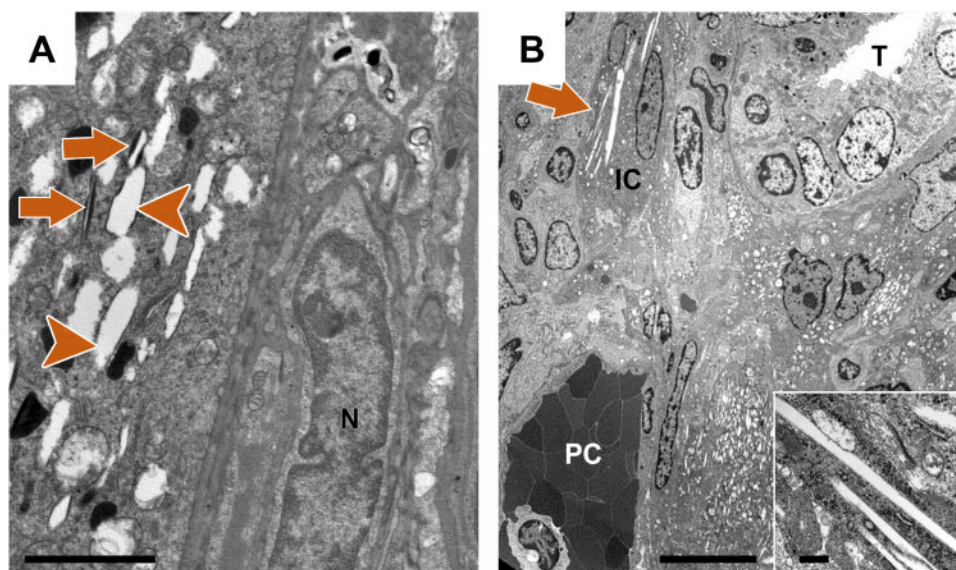


Figure 7. Confirmation of crystal deposit presence by electron microscopy of the eyes and kidneys. A, Eye of a male rat treated with RO0728617 at 90/70/90 mg/kg/day for 8 weeks showing the pigment epithelium with intracellular crystal clefts surrounded by membranes (arrowheads) and single dark staining melanosomes with crystal clefts (arrows). Abbreviation: N, nucleus, scale bar = 2 μm . B, Kidney of a male rat treated with RO0728617 at 90 mg/kg/day for 28 days showing part of the tubular-interstitial space with interstitial cell infiltrates (macrophages). One interstitial cell (IC) is shown with numerous intracytoplasmic crystals (arrow), peritubular capillary (PC) and tubules (T) are unremarkable. Scale bar = 10 μm . Intracellular crystals without clear-cut surrounding membrane are shown in the inset at 20-fold higher magnification. Scale bar = 500 nm.

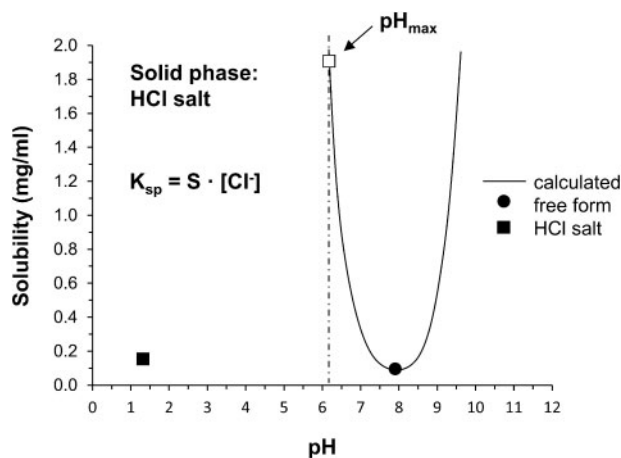


Figure 8. Calculated pH-solubility profile of RO0728617 (free form) based on a measured solubility of 0.090 mg/ml at pH 7.96 (closed circle) and the compound's basic pKa of 8.6 and acidic pKa of 7.2. The closed square represents the measured solubility of the RO0728617-hydrochloride (HCl) formed in 0.1 M hydrochloric acid. The open square shows the calculated pH of maximum solubility of the RO0728617-HCl salt (pH_{max}).

concentrations (108 mM) was 0.071 mg/ml. At a lysosomal pH of approximately 5.0, the equilibrium solid form species was RO0728617-HCl salt. A detailed description for the calculation of the estimated values based on measured solubility data can be found in the [Supplementary Material](#).

Estimation of Compound Concentration in Lysosomes Based on Total Plasma Concentration

The concentration of RO0728617 within lysosomes can be estimated based upon the pH-partition equation, assuming that passive permeability is high, that the compound is equally distributed under steady-state conditions, and that uptake or efflux transport systems have no major impact on the disposition of the compound within the organs analyzed. Based on the pKa values of the compound, and the difference in pH values in the cytosol and the lysosomes, a ratio of the unbound concentration ($K_p, u_{u, lyso}$) between the lysosome and the cytosol can be calculated. Due to the pH differences between the lysosomes and the cytosol, free compound concentration in the lysosome ($C_{Lyso, u}$) was calculated to be 100-fold higher than in the cytosol. If we assume an equal pH between the cytosol and plasma, free compound concentration in the cytosol is also 100-fold higher than the free concentration measured in plasma (Table 2 and Figure 9). This relationship between the pKa values of the compound and differences in organelle pH allows concentration estimation with the toxicokinetic information summarized in Table 2; an estimation of the concentration in the lysosomes at C_{max} (maximal concentration) and the average concentration at steady state (C_{ss}). A comparison with the estimated solubility under physiological-like conditions in the lysosomes showed that free unbound concentration in the lysosomes ($C_{Lyso, u}$) is below the solubility limit for the lowest dose (15 mg/kg), whereas the mid-dose (45 mg/kg) leads to concentrations that are in the range of the solubility limit of the compound; for the high dose (90 mg/kg) concentrations are above the solubility limit (Table 2).

DISCUSSION

Toxicity studies with RO0728617, an amphoteric compound bearing basic and acidic moieties, have revealed widespread

Table 2. Estimated Concentration of RO0728617 in the Cytosol and Lysosome at Different Doses After 14 Days of Dosing

Dose (mg/kg/day)	Dose (mmol/kg/day)	C_{max} (ng/ml)	$C_{cyto, u}$ at C_{max} (ng/ml)	$C_{Lyso, u}$ at C_{max} (ng/ml)	$C_{Lyso, u}$ at C_{max} /Estimated Solubility in Lysosome	C_{ss} (ng/ml)	$C_{cyto, u}$ at C_{ss} (ng/ml)	$C_{Lyso, u}$ at C_{ss} (ng/ml)	$C_{Lyso, u}$ at C_{ss} /Estimated Solubility in Lysosome
15	0.033	6382	485	48 500	0.68	3953	300	30 000	0.43
45	0.100	26 392	2006	200 600	2.8	13 424	1020	10 2000	1.5
90	0.200	25 366	1928	192 800	2.7	16 545	1257	12 5700	1.8

Red color indicates that the solubility is lower than estimated lysosomal concentration, green indicates that the solubility is higher than the lysosomal concentration. Fraction unbound in rat plasma ($f_u, plasma$) = 7.6%. Estimated solubility in lysosomes = 71 000 ng/ml (71 μ g/ml).

Abbreviations: $C_{cyto, u}$, concentration in cytosol; $C_{Lyso, u}$, concentration in lysosomes; C_{max} , maximal concentration; C_{ss} , steady-state concentration.

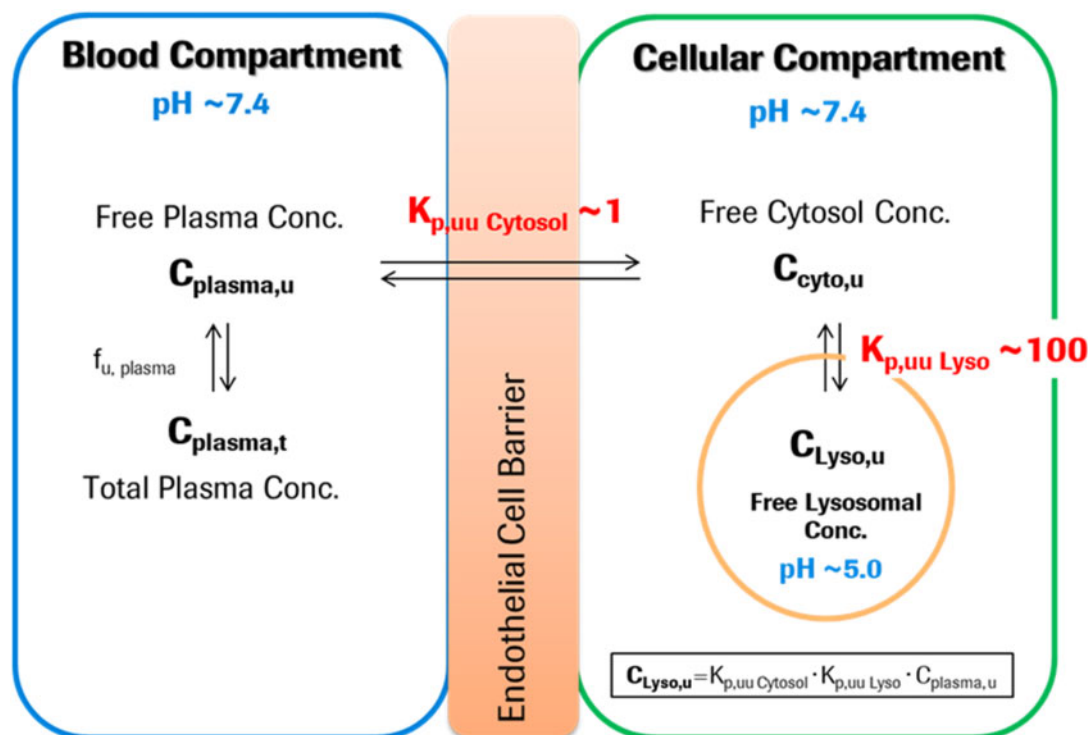


Figure 9. Schematic representation of the pH dependent partitioning of the amphoteric compound RO0728617 between blood plasma, the intracellular compartment and the lysosome. Abbreviations: $C_{\text{cyto,u}}$, free compound concentration in the cytosol; $C_{\text{Lyso,u}}$, free lysosomal concentration; $C_{\text{plasma,u}}$, free plasma concentration; $C_{\text{plasma,t}}$, total plasma concentration; $f_{\text{u, plasma}}$, fraction unbound in plasma; $K_{\text{p,uu Cytosol}}$, the unbound drug partitioning coefficient of the cytosol; $K_{\text{p,uu Lyso}}$, unbound drug partitioning coefficient of the lysosome.

crystal deposition in multiple tissues. Microscopic features were unusual, with associated macrophage infiltrates appearing as fibrillary structures with scattered nuclei. CD68 IHC confirmed that these lesions consisted of macrophage aggregates containing crystal clefts. Foamy/vacuolated macrophages were also observed in the lungs and mesenteric lymph node, suggestive of macrophage uptake or activation; MALDI-FTICR MS imaging revealed that the crystals were composed of the orally administered compound. Spectroscopic techniques confirmed that these crystals consisted of the crystalline HCl salt compound form, as previously described (Lenz et al., 2018). Electron microscopic examination of the eye and kidney revealed intracellular crystalline structures, although the exact subcellular localization could not always be determined. In the pigment epithelium of the retina, some crystals were located within melanosomes, whereas others were membrane-bound, suggestive of lysosomal localization. In the kidney, membrane-bound crystals were not consistently observed by EM; however, Lamp2 IHC did suggest lysosomal localization. The presence of foamy/vacuolated macrophages preceding the deposition of crystals in multiple tissues suggest macrophage uptake as a primary toxicity event. Crystal deposits occur when solubility limits are reached, eg, due to high local concentrations of exogenous or endogenous substances, and also as a consequence of pH changes at the tissue or subcellular level, in association with substance solubility differences at different pHs. Renal crystal deposits are commonly seen as a consequence of drug insolubility in renal tubules at alkaline or acidic urine pH (Yarlagadda and Perazella, 2008).

It was recently reported that for an orally administered, weakly basic molecule, with pH-dependent solubility, low solubility at neutral pH, and high permeability, crystallization risk is

likely highest at the site of absorption where it first encounters the physiological pH, but is also likely in other organs (Ruepp et al., 2019). Ruepp et al. (2019), concluded that compounds with intrinsic solubility $\leq 1 \mu\text{g/ml}$ have a higher risk of crystal formation *in vivo*. Other authors found that oral uptake of clofazimine, a weak base that is poorly soluble at higher pH, can lead to formation of supersaturated solutions when it passes from the acidic pH of the stomach to the less acidic pH of the intestine (Baik and Rosania, 2012). In humans, extra-renal crystal deposits have been reported in the gastro-intestinal mucosa after oral uptake of sevelamer and other ion-exchange resins (Desai et al., 2016; Yuste et al., 2017). A number of other compounds, such as tamoxifen, canthaxanthin, talc and nitrofurantoin, have also been reported to induce crystal deposits in humans within the eye (Nadim et al., 2001). In primary oxalosis as well as in cystinosis, crystals are not only found in the kidney but also in other tissues (Bhasin et al., 2015; Cochat and Rumsby 2013).

In this study, the lysosomal accumulation potential of RO0728617 was estimated by a simple method based upon its physicochemical properties. This was done under the assumption that at steady-state conditions, the disposition of the compound within the cells is solely affected by the pH gradient between the plasma, cytosol, and lysosomes. This, therefore, means that the compound has to have a sufficiently high passive permeability, with no uptake or efflux transporters involved in the relocalization of the molecule. The estimated concentration within the lysosomes suggests that lysosomal accumulation occurs with subsequent precipitation at higher doses, and consequently the observation of multiorgan crystal deposits.

Lysosomes have 2 major physicochemical characteristics; a lower pH (5.0) compared with the cytosol (approximately 7.2)

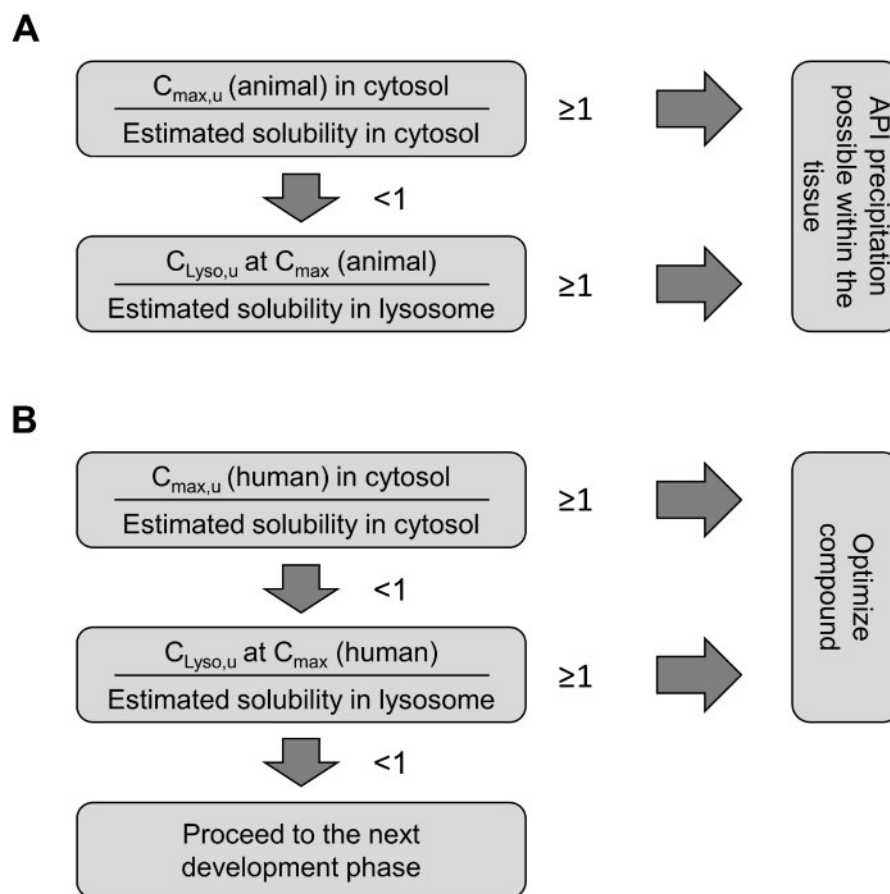


Figure 10. A, Flowchart describing the evaluation process of pre-clinical animal studies. When the ratio of $C_{\max, u}$ in the cytosol/estimated solubility in the cytosol is higher or equal to 1, the likelihood that the compound precipitates within tissues is high, which may lead to a visible or invisible compound precipitation. Due to the accumulation of API in the lysosome, the $C_{\text{Lyso}, u}$ at C_{\max} may exceed the estimated solubility in lysosome, which may also lead to API precipitation within the tissue. B, Flowchart describing the evaluation process at the level of the expected human therapeutic dose. In the preclinical phase, the human C_{\max} can be estimated with physiological-based pharmacokinetic modeling based on the available human *in vitro* data (Miller et al., 2019). When the ratio of $C_{\max, u}$ in the cytosol/estimated solubility in the cytosol is ≥ 1 , the likelihood that the compound precipitates within human tissues is high and the compound should be further optimized in the preclinical phase. If the ratio is < 1 , it should be checked if $C_{\text{Lyso}, u}$ at C_{\max} may exceed the estimated solubility in lysosome, which may lead to API precipitation within the human tissue. In this scenario, the compound should be optimized in the pre-clinical phase. Only if both ratios are < 1 should the compound proceed to the next development phase. Abbreviations: API, active pharmaceutical ingredient; C_{\max} (animal), maximal plasma concentration of the preclinical animal study; C_{\max} (human), maximal plasma concentration at the expected human therapeutic dose; $C_{\max, u}$, unbound concentration at C_{\max} ; $C_{\text{Lyso}, u}$, unbound concentration in lysosomes at C_{\max} .

and high chloride concentration (approximately 108 mM) compared with the cytosol (approximately 45 mM; Sonawane et al., 2002; Trehame et al., 2006). The low pH in lysosomes leads to an accumulation of basic amphiphilic compounds in the inner leaflet of negatively charged lysosomal lipid membranes, where they may impede the function of phospholipases with the consequence of an intracellular lipid accumulation and phospholipidosis (Shayman et al., 2011). We hypothesize that basic, non-, or poorly amphiphilic compounds can also accumulate in lysosomes without intercalating with the lipid membrane and thus, without impeding any physiologically relevant mechanism in the lysosomal membrane. RO0728617 is amphoteric, which means that it has a weak acidic moiety (pK_a 7.2) in addition to its basic center. Under the slightly acidic conditions experienced within lysosomes the acidic group is fully protonated, and so the compound behaves like a basic compound, leading to a 100-fold drug accumulation compared with the cytosolic cell compartment. In addition, there is a substantial solubility difference between the free form of RO0728617 (32.2 mg/ml at pH 5.0) and the HCl salt (0.071 mg/ml) in lysosomes. Both effects, lysosomal accumulation and the decrease in solubility at lysosomal

chloride concentrations, may allow precipitation of the poorly soluble HCl salt within the lysosomes.

The hypothesis of lysosomal accumulation was further supported by the morphologic changes noted in our studies, which show similarities to those described after administration of clofazimine (Mamidi et al., 1995), or in association with systemic cystinosis (Cherqui et al., 2002; Elmonem et al., 2016). Clofazimine is a CAD compound with moderate amphiphilicity for which crystal-like drug inclusions of the clofazimine-HCl form have been observed in tissue macrophages (Keswani et al., 2015). Interestingly, it was shown that these crystals were formed *in vitro* at pH 5.0; the same conditions that exist in lysosomes (de Duve et al., 1974). Crystal-like inclusions were reported to be surrounded by multilamellar membrane structures; accumulation in lysosomes or endosomes was considered but the precise identity of the organelle involved could not be determined (Keswani et al., 2015). It has also been shown that a number of basic amphiphilic tyrosine kinase inhibitors accumulate and precipitate in lysosomes *in vivo* (Fu et al., 2014); when the local concentration exceeds the solubility limit, the compound may precipitate in different forms and can occur in the

form of crystals that can be seen under polarized light (as described here). However, the compound can remain in a supersaturated state where it does not precipitate, or it may precipitate in the form of small aggregates/particles that are practically invisible by light microscopy.

In the case of the hereditary cystinosis, lysosomal storage of cystine occurs due to a defect in the membrane transport protein, cystinosis (Nesterova and Gahl, 2013). Cystine is poorly soluble and forms crystals as its concentration increases, which accumulate in all cells and tissues (Elmonem et al., 2016). In mice lacking cystinosis, cystine crystals are seen within interstitial cells of various organs (Cherqui et al., 2002). In the human kidney, cystine crystals have been noted to occur in the cortical interstitium within macrophages (as in our study) but also in tubular and glomerular epithelial cells (Lusco et al., 2017). Electron microscopic examination confirmed the cystine crystals were localized within lysosomes (Iancu et al., 1987; Schulman et al., 1970). Iancu et al., (1987) discussed this compartmentalization of cystine within lysosomes as the primary manifestation, which is in line with our hypothesis, although we did not confirm lysosomal localization for all crystals. In this study, several crystals were found intracellularly but without a clear surrounding membrane, particularly in the kidney. This could be explained by crystal size and the destruction of lysosomal integrity (Sun et al., 2017). Tubular uptake of our compound with subsequent accumulation and precipitation, followed by macrophage uptake in the renal interstitium, was considered unlikely because Lamp2 IHC did not reveal any difference in tubular staining between control and treated animals. The presence of crystals in melanosomes of the pigment epithelium was not surprising as they are lysosome-related organelles (Wasmeier et al., 2008) and can have an acidic pH (Bhatnagar et al., 1993). Taken together, all available data indicate lysosomal accumulation as the primary event and compound precipitation as a consequence of reaching solubility limit. Our results show that despite good solubility at physiological pH, compounds with amphoteric properties and a positive net charge may accumulate and subsequently precipitate in the acidic environment of lysosomes, leading to multiorgan toxicity.

In conclusion, our investigations demonstrated that treatment with an amphoteric drug, which has good solubility at physiological pH, resulted in crystal deposition consisting of the HCl salt form of the RO0728617 compound in multiple tissues. The precipitation was explained by lysosomal accumulation of the compound (free form), followed by conversion to the poorly soluble HCl salt at lysosomal pH, and the 2-fold higher chloride concentration compared with the cytosol. Based on our explanations above, we speculate that precipitation of the HCl salt may reduce the intralysosomal chloride concentration, which may impair lysosomal function. Lysosomal accumulation potential of drug candidates can be estimated by a simple method based on the physicochemical properties of the compound. The miniaturized InSiSa screening method, as used herein, is useful to evaluate the existence of a poorly soluble HCl salt of basic or amphoteric compounds. This has practical applications for improving drug discovery (Figure 10); with a minimal number of basic parameters (ionization constants [pKa], pH-solubility profile, pH_{max} and solubility product [parameters explained in the Supplementary Material], protein binding, and plasma exposure) it is possible to quickly check if lysosomal HCl salt precipitation may occur.

SUPPLEMENTARY DATA

Supplementary data are available at Toxicological Sciences online.

ACKNOWLEDGMENTS

We would like to thank Dr Rodolfo Gasser for providing the plasma exposure data and for reviewing the article. We would like to thank Petra Stäuble and Rachel Neff for the technical support, and Meridian HealthComms for editorial support, which was funded by F. Hoffmann-La Roche Ltd.

FUNDING

Roche Pharma Research and Early Development, F. Hoffmann-La Roche Ltd, Basel, Switzerland.

DECLARATION OF CONFLICTING INTERESTS

All authors, except M.J.M., are employees of F. Hoffmann-La Roche Ltd. M.J.M. reports no conflicts of interest.

REFERENCES

- Aziz, R., and Helms, W. (2009). Pharmacology/toxicology review and evaluation: Pazopanib. Available at: https://www.accessdata.fda.gov/drugsatfda_docs/nda/2009/022465s000_PharmR.pdf. Accessed March 23, 2020.
- Baik, J., and Rosania, G. (2012). Macrophages sequester clofazimine in an intracellular liquid crystal-like supramolecular organization. *PLoS One* 7, e47494.
- Bhasin, B., Urekli, H., and Atta, M. (2015). Primary and secondary hyperoxaluria: Understanding the enigma. *World J. Nephrol.* 4, 235–244.
- Bhatnagar, V., Anjaiah, S., Puri, N., Darshanam, B., and Ramaiah, A. (1993). pH of melanosomes of B 16 murine melanoma is acidic: Its physiological importance in the regulation of melanin biosynthesis. *Arch. Biochem. Biophys.* 307, 183–192.
- Boyd, B. J., Bergström, C. A. S., Vinarov, Z., Kuentz, M., Brouwers, J., Augustijns, P., Brandl, M., Bernkop-Schnürch, A., Shrestha, N., Préat, V., et al. (2019). Successful oral delivery of poorly water-soluble drugs both depends on the intraluminal behavior of drugs and of appropriate advanced drug delivery systems. *Eur. J. Pharm. Sci.* 137, 104967.
- Brouwers, J., Brewster, M. E., and Augustijns, P. (2009). Supersaturating drug delivery systems: The answer to solubility-limited oral bioavailability? *J. Pharm. Sci.* 98, 2549–2572.
- Chatman, L. A., Morton, D., Johnson, T. O., and Anway, S. D. (2009). A strategy for risk management of drug-induced phospholipidosis. *Toxicol. Pathol.* 37, 997–1005.
- Cherqui, S., Sevin, C., Hamard, G., Kalatzis, V., Sich, M., Pequignot, M. O., Gogat, K., Abitbol, M., Broyer, M., Gubler, M. C., et al. (2002). Intralysosomal cystine accumulation in mice lacking cystinosis, the protein defective in cystinosis. *Mol. Cell. Biol.* 22, 7622–7632.
- Cochat, P., and Rumsby, G. (2013). Primary hyperoxaluria. *N. Engl. J. Med.* 369, 649–658.

- de Duve, C., de Barsey, T., Poole, B., Trouet, A., Tulkens, P., and Van Hoof, F. (1974). Commentary. Lysosomotropic agents. *Biochem. Pharmacol.* **23**, 2495–2531.
- Desai, M., Reiprich, A., Khov, N., Yang, Z., Mathew, A., and Levenick, J. (2016). Crystal-associated colitis with ulceration leading to hematochezia and abdominal pain. *Case Rep. Gastroenterol.* **10**, 332–337.
- Elmonem, M. A., Veys, K. R., Soliman, N. A., van Dyck, M., van den Heuvel, L. P., and Levchenko, E. (2016). Cystinosis: A review. *Orphanet J. Rare Dis.* **11**, 47.
- Fischer, H., Atzpodien, E. A., Csato, M., Doessegger, L., Lenz, B., Schmitt, G., and Singer, T. (2012). In silico assay for assessing phospholipidosis potential of small druglike molecules: Training, validation, and refinement using several data sets. *J. Med. Chem.* **55**, 126–139.
- Friden, M., Bergstrom, F., Wan, H., Rehngrén, M., Ahlin, G., Hammarlund-Udenaes, M., and Bredberg, U. (2011). Measurement of unbound drug exposure in brain: Modeling of pH partitioning explains diverging results between the brain slice and brain homogenate methods. *Drug Metab. Dispos.* **39**, 353–362.
- Fu, D., Zhou, J., Zhu, W. S., Manley, P. W., Wang, Y. K., Hood, T., Wylie, A., and Xie, X. S. (2014). Imaging the intracellular distribution of tyrosine kinase inhibitors in living cells with quantitative hyperspectral stimulated Raman scattering. *Nat. Chem.* **6**, 614–622.
- Iancu, T. C., Lerner, A., and Shiloh, H. (1987). Intestinal mucosa in nephropathic cystinosis. *J. Pediatr. Gastroenterol. Nutr.* **6**, 359–364.
- Keswani, R. K., Baik, J., Yeomans, L., Hitzman, C., Johnson, A. M., Pawate, A. S., Kenis, P. J. A., Rodriguez-Hornedo, N., Stringer, K. A., and Rosania, G. R. (2015). Chemical analysis of drug biocrystals: A role for counterion transport pathways in intracellular drug disposition. *Mol. Pharm.* **12**, 2528–2536.
- Lenz, B., Brink, A., Siam, M., De Paepe, A., Bassett, S., Eichinger-Chapelon, A., Maliver, P., Neff, R., Niederhauser, U., Steinhuber, B., et al. (2018). Application of imaging techniques to cases of drug-induced crystal nephropathy in preclinical studies. *Toxicol. Sci.* **163**, 409–419.
- Logan, R., Funk, R. S., Axcell, E., and Krise, J. P. (2012). Drug-drug interactions involving lysosomes: Mechanisms and potential clinical implications. *Expert Opin. Drug Metab. Toxicol.* **8**, 943–958.
- Lüllmann, H., and Lüllmann-Rauch, R. (1981). Tamoxifen-induced generalized lipidosis in rats subchronically treated with high doses. *Toxicol. Appl. Pharmacol.* **61**, 138–146.
- Lusco, M. A., Najafian, B., Alpers, C. E., and Fogo, A. B. (2017). AJKD Atlas of Renal Pathology: Cystinosis. *Am. J. Kidney Dis.* **70**, e23–e24.
- Mamidi, N. V., Rajasekhar, A., Prabhakar, M. C., and Krishna, D. R. (1995). Tissue distribution and deposition of clofazimine in rat following subchronic treatment with or without rifampicin. *Arzneimittelforschung* **45**, 1029–1031.
- Miller, N. A., Reddy, M. B., Heikkinen, A. T., Lukacova, V., and Parrott, N. (2019). Physiologically based pharmacokinetic modelling for first-in-human predictions: An updated model building strategy illustrated with challenging industry case studies. *Clin. Pharmacokinet.* **58**, 727–746.
- Nadim, F., Walid, H., and Adib, J. (2001). The differential diagnosis of crystals in the retina. *Int. Ophthalmol.* **24**, 113–121.
- Nasr, S. H., Milliner, D. S., Wooldridge, T. D., and Sethi, S. (2014). Triamterene crystalline nephropathy. *Am. J. Kidney Dis.* **63**, 148–152.
- Nesterova, G., and Gahl, W. A. (2013). Cystinosis: The evolution of a treatable disease. *Pediatr. Nephrol.* **28**, 51–59.
- Nie, H., Byrn, S. R., and Zhou, Q. (2017). Stability of pharmaceutical salts in solid oral dosage forms. *Drug Dev. Ind. Pharm.* **43**, 1215–1228.
- Ruepp, S., Janovitz, E., Brodie, T., White, R., Santella, J., Hynes, J., Carman, J., Pan, D., Wu, Y., Hanumegowda, U., et al. (2019). Assessing the risk of drug crystallization in vivo. *J. Pharmacol. Toxicol. Methods* **96**, 1–8.
- Schulman, J. D., Wong, V., Olson, W. H., and Seegmiller, J. E. (1970). Lysosomal site of crystalline deposits in cystinosis as shown by ferritin uptake. *Arch. Pathol.* **90**, 259–264.
- Shayman, J. A., Kelly, R., Kollmeyer, J., He, Y., and Abe, A. (2011). Group XV phospholipase A2, a lysosomal phospholipase A2. *Prog. Lipid Res.* **50**, 1–13.
- Sonawane, N. D., Thiagarajah, J. R., and Verkman, A. S. (2002). Chloride concentration in endosomes measured using a ratioable fluorescent Cl⁻ indicator: Evidence for chloride accumulation during acidification. *J. Biol. Chem.* **277**, 5506–5513.
- Soukup, P., Lenz, B., Altmann, B., Badillo, S., Atzpodien, E.-A., and Pot, S. A. (2020). Combined cSLO-OCT imaging as a tool in preclinical ocular toxicity testing: A comparison to standard in-vivo and pathology methods. *J. Pharmacol. Toxicol. Methods* **104**, 106873.
- Stoekli, M., Staab, D., Wetzel, M., and Brechbuehl, M. (2014). iMatrixSpray: A free and open source sample preparation device for mass spectrometric imaging. *Chimia (Aarau)* **68**, 146–149.
- Sun, X. Y., Gan, Q. Z., and Ouyang, J. M. (2017). Size-dependent cellular uptake mechanism and cytotoxicity toward calcium oxalate on Vero cells. *Sci. Rep.* **7**, 41949.
- Tong, W.-Q. T., and Whitesell, G. (1998). In situ salt screening - A useful technique for discovery support and preformulation studies. *Pharm. Dev. Technol.* **3**, 215–223.
- Treharne, K. J., Crawford, R. M., and Mehta, A. (2006). CFTR, chloride concentration and cell volume: Could mammalian protein histidine phosphorylation play a latent role? *Exp. Physiol.* **91**, 131–139.
- Wagner, B., Fischer, H., Kansy, M., Seelig, A., and Assmus, F. (2015). Carrier Mediated Distribution System (CAMDIS): A new approach for the measurement of octanol/water distribution coefficients. *Eur. J. Pharm. Sci.* **68**, 68–77.
- Wasmeier, C., Hume, A. N., Bolasco, G., and Seabra, M. C. (2008). Melanosomes at a glance. *J. Cell Sci.* **121**, 3995–3999.
- Yarlagadda, S. G., and Perazella, M. A. (2008). Drug-induced crystal nephropathy: An update. *Expert Opin. Drug Saf.* **7**, 147–158.
- Yuste, C., Merida, E., Hernandez, E., Garcia-Santiago, A., Rodriguez, Y., Munoz, T., Gomez, G. J., Sevillano, A., and Praga, M. (2017). Gastrointestinal complications induced by sevelamer crystals. *Clin. Kidney J.* **10**, 539–544.